First-Principles Calculations of Exciton Radiative Lifetimes in Monolayer Graphitic Carbon Nitride Nanosheets: Implications for Photocatalysis

(Article begins on next page)

25 April 2024

Article

First-Principles Calculations of Exciton Radiative Lifetimes in Monolayer Graphitic Carbon Nitride Nanosheets: Implications for Photocatalysis

Michele Re Fiorentin,* Francesca Risplendi, Maurizia Palummo, and Giancarlo Cicero

Read Online

ACCESS | Metrics & More | Article Recommendations | SI Supporting Information

ABSTRACT: In this work, we report on the exciton radiative lifetimes of graphitic carbon nitride monolayers in the triazine-based (gC_3N_4-t) and heptazine-based (gC_3N_4-h) forms, as obtained by means of ground-state plus excited-state *ab initio* calculations. By analyzing the exciton fine structure, we highlight the presence of dark states and show that the photogenerated electron−hole (e-h) pairs in gC_3N_4-h are remarkably long-lived, with an effective radiative lifetime of 260 ns. This fosters the employment of gC_3N_4-h in photocatalysis and makes it attractive for the emerging field of exciton devices. Although very long intrinsic radiative lifetimes are an important prerequisite for several applications, pristine carbon nitride nanosheets show very low quantum photoconversion efficiency, mainly due to the lack of an efficient e-h separation mechanism. We then focus on a vertical heterostructure made of gC_3N_4-t and gC_3N_4-h layers, which shows a type-II band alignment and looks promising for achieving net charge separation.

KEYWORDS: carbon nitride, excitons, 2D materials, radiative lifetimes, heterostructures
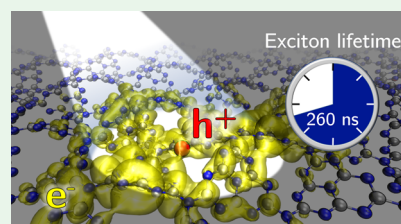
1. INTRODUCTION

After the seminal work of Wang et al.[1] in 2009, proposing polymeric graphitic carbon nitride as a new, eco-friendly, low cost, and thermally stable photocatalyst for hydrogen evolution, this layered material has become the subject of intense research efforts[2−9] for possible employment in several applications[10−12] as a "green" replacement of more expensive, polluting, metal-containing compounds.[13−18] Among various allotropes of C_3N_4 with different densities,[19−21] the graphitic form has been proved to be the most stable at standard conditions.[22] It is composed of two-dimensional (2D) layers of carbon and nitrogen atoms covalently bonded, stacked by means of van der Waals (vdW) interactions as in graphite. These weak dispersion forces allow to easily exfoliate graphitic carbon nitride[23,24] into few-layers nanosheets or even single-layer, graphene-like carbon nitride (gC_3N_4). gC_3N_4 single layers can be built from either triazine or heptazine (tri-*s*-triazine) molecules as basic units, forming, respectively, the so-called triazine- (gC_3N_4-t) or heptazine-based (gC_3N_4-h) graphene-like carbon nitride.

Most of the experimental works on pristine graphitic carbon nitride investigate the optoelectronic properties and address the carrier dynamics with the goal of understanding the origin of the low photoconversion efficiency.[25−28] Typical lifetimes of the photogenerated electron−hole pairs, measured in nanosheets with thickness ranging from few to several nanometers, are of the order of few nanoseconds, with values that change depending on the sample preparation and thickness.[29−34]

On the theoretical side, a large number of *ab initio* studies, at different levels of approximation, have been carried out to clarify the structural, electronic, and optical properties both of the bulk and the monolayer form.[35−40] Thanks to these studies, it is now clear that the most stable atomic structure is buckled[41−44] and that corrugation, by breaking the delocalized π-bond, significantly alters the electronic and excitonic optical properties from those calculated for the flat, unstable structures. However, different corrugated geometries have been proposed and a complete description of the fundamental properties of both gC_3N_4-t and gC_3N_4-h, encompassing optical spectra, exciton fine structure, and intrinsic radiative lifetimes is, to our knowledge, still lacking.

Our aim is therefore to provide a thorough study of the electronic, optical, and excitonic properties of both gC_3N_4-t and gC_3N_4-h in the buckled geometries without dynamical instabilities. This preliminary structural optimization, performed using density functional theory (DFT) simulations, enables us to reliably predict the quasi-particle (QP) electronic structures of both allotropes at the state-of-the-art GW[45−47] level. Our study shows that the effect of corrugation on the electronic properties is sizeable both at the DFT and GW level of approximation. While this behavior has been already discussed in the literature, as we will point out in the
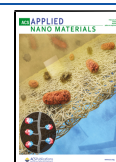
following, our QP bandgaps present significant differences with previously published data. The optical properties, obtained by solving the Bethe−Salpeter equation (BSE),[48,49] are characterized by pronounced excitonic effects associated to a rich structure of dark and bright strongly bound excitons, widely influenced by corrugation.

Thanks to a recently derived approach,[50,51] we compute, for both materials, the intrinsic exciton radiative lifetimes and their effective average, showing that gC$_3$N$_4$-h is characterized by a significantly long effective radiative lifetime. By suppressing electron−hole recombination, long exciton lifetimes can increase the chances of exciton dissociation and enhance the photocatalytic activity.[52−54] Moreover, excited states with long lifetimes can be particularly suitable for study and manipulation in external electromagnetic fields, as in the emerging domain of excitonic devices.[55−59]

To overcome the small availability of photogenerated free carriers, due to the large binding energies, exciton dissociation must be improved. Several mechanisms to achieve this goal have been proposed, ranging from doping with metal and non-metal atoms,[60,61] to order−disorder transitions,[62] to the creation of heterojunctions.[63−65] We show that a novel vdW heterostructure, in which a gC$_3$N$_4$-t and a gC$_3$N$_4$-h layer are vertically stacked, results in an interface with a type-II band alignment, promising for obtaining net charge separation between the two layers.

In the quest for a deeper knowledge of this intriguing 2D material and for devising new applications in various fields, ranging from optoelectronics,[66−69] to electrocatalysis,[42,70,71] to photocatalysis,[72−75] a detailed description and comparison of the electronic, optical, and excitonic properties is essential. Our results aim at providing such a resource, which can prove helpful in the understanding gC$_3$N$_4$ features and in the design of new technological applications.

The paper is organized as follows: in Section 2, we present the computational methods used to carry out our study; in Section 3, we discuss the results; and finally, in Section 4, we draw the conclusions.

2. METHODS

Structural optimizations are performed by means of DFT simulations carried out with the Quantum ESPRESSO package.[76,77] At this level of approximation, the gradient corrected Perdew−Burke−Ernzerhof (PBE) functional[78] is employed to describe the exchange-correlation effects, and norm-conserving pseudopotentials[79] are used to model the electron−ion interactions. Wavefunctions are expanded in plane waves up to an energy cutoff of 80 Ry. To study various degrees of buckling, we employ different cells for both allotropes. We consider the standard unit cell, 1 × 1, of gC$_3$N$_4$-t (gC$_3$N$_4$-h), comprising 7 (14) atoms (cf. Figure 1), supercells obtained by its repetition along the lattice plane, such as 2 × 2 and 4 × 4 supercells, and rotated $\sqrt{3} \times \sqrt{3}$ cells, as shown in Figure 1, containing 21 and 42 atoms for gC$_3$N$_4$-t and gC$_3$N$_4$-h, respectively. In the case of the standard 1 × 1 cells, the Brillouin zone is sampled using a 4 × 4 × 1 Monkhorst−Pack mesh[80] for gC$_3$N$_4$-t and a 2 × 2 × 1 mesh for gC$_3$N$_4$-h. For the $\sqrt{3} \times \sqrt{3}$ cells, calculations are performed on a 2 × 2 × 1 mesh for gC$_3$N$_4$-t and at the Γ point for gC$_3$N$_4$-h. vdW interactions are treated within the semiempirical Grimme-D3 approach,[81] and a vacuum region at least 15 Å thick along the direction orthogonal to the atomic layer is used to ensure the decoupling of the periodic replicas.

Dynamical stability of the obtained structures is assessed through the calculation of their phonon density of states (phDOS).[82] The presence of modes with imaginary frequencies is a sign that the considered structure, though an energy stationary point, tends to collapse to more stable geometries. phDOS are obtained with the
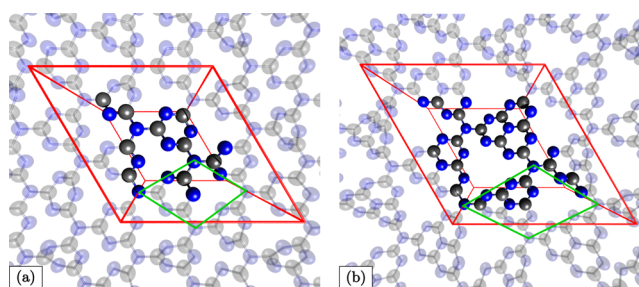
Figure 1. (a, b) Perspective views of the optimized geometries of gC$_3$N$_4$-t and gC$_3$N$_4$-h, respectively. The $\sqrt{3} \times \sqrt{3}$ cells are marked with solid red lines, while the standard 1 × 1 cells with thinner, green lines. Carbon and nitrogen atoms are represented by gray and blue spheres, respectively.

PHONOPY code,[83] which employs a supercell, frozen-phonon approach. The dynamically stable, equilibrium geometries are then used for further calculations of their electronic and optical properties.

It is well known that DFT fails at properly describing the electronic structure and bandgap of semiconductors and insulators. To obtain precise results on the band structure and electronic gap, many-body perturbation theory techniques must be used. In this work, many-body corrections are calculated within the non-self-consistent perturbative GW (G_0W_0) approximation, as implemented in the YAMBO code.[84,85] The vacuum thickness is increased to 20 Å, and a box cutoff along the direction orthogonal to the lattice plane is employed. Bruneval−Gonze terminators[86] are used in the calculation of both the susceptibility and the correlation self-energy, and the plasmon-pole approximation is adopted. Convergence with respect to the free parameters of the theory is assumed when the value of the QP bandgap at the Γ point varies less than 50 meV. Following this criterion, an 8 × 8 × 1 (6 × 6 × 1) k-point mesh is used for gC$_3$N$_4$-t (gC$_3$N$_4$-h).

We followed a "ladder" convergence method as laid out in ref 87, obtaining converged results with 400 (800) bands for gC$_3$N$_4$-t (gC$_3$N$_4$-h) and a dielectric matrix energy cutoff of 20 Ry for both allotropes. More details on the convergence procedure are available in the Supporting Information. Reliable optical properties can then be obtained by solving the BSE using the obtained QP corrections and adopting the Tamm−Dancoff approximation.[88,89] Converged spectra are computed within the static exchange approximation on denser 18 × 18 × 1 and 9 × 9 × 1 grids, using 150 and 300 bands for gC$_3$N$_4$-t and gC$_3$N$_4$-h, respectively, and a 2 Ry cutoff on the dielectric matrix for both materials. Once the BSE is solved, we compute the radiative lifetime, τ_S, of each exciton state S at **Q** = 0 using Fermi's golden rule.[50,51,90] For Wannier excitons, the exciton dispersion in **Q** could be taken into account and the radiative lifetime renormalized by a thermal average on **Q**, assuming a parabolic dispersion. However, as shown in the following section, in our cases the bands involved in the relevant exciton states are almost flat in the neighborhood of the k points where the most significant transitions take place. This, in turn, causes a negligible exciton dispersion, which does not justify a thermal average over finite **Q** inside the light cone. Therefore, in what follows we shall employ the exciton radiative lifetimes calculated at **Q** = 0 and obtain the effective radiative lifetime, $\langle \tau \rangle_{eff}$, at temperature T, by assuming thermalization and carrying out a Boltzmann average of the τ_S.[91]

Finally, the unit cell of the vdW heterostructure made of a gC$_3$N$_4$-t and a gC$_3$N$_4$-h layer is obtained from the respective optimized $\sqrt{3} \times \sqrt{3}$ cells by means of the CellMatch code.[92]

3. RESULTS AND DISCUSSION

We begin our study by comparing the stability of different gC$_3$N$_4$ structures built from the standard 1 × 1 cell and the $\sqrt{3} \times \sqrt{3}$ cell. The flat 1 × 1 cells are included in our study as references. When addressing buckling, the 1 × 1 cells show
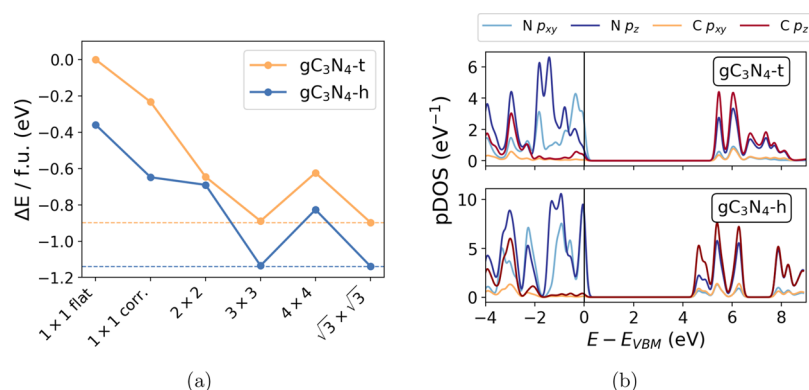
Figure 2. (a) Energy per formula unit (f.u.) of gC_3N_4-t and gC_3N_4-h in different simulation cells, referenced to flat $1 \times 1 gC_3N_4$-t. (b) Projected density of states of gC_3N_4-t (top panel) and gC_3N_4-h (bottom panel).

some level of corrugation; however, due to the periodic boundary conditions, they impose strong constraints on the atom positions. By considering larger supercells, such as 2×2, etc., artificial constraints on the geometry are gradually lifted, and the atomic layers acquire different degrees of corrugation. The buckling is due to the strong electrostatic repulsion between the lone pairs of the pyridinic-like nitrogen atoms that surround the void triangular regions in the atomic layer. Lifting geometrical constraints allows for a certain degree of relaxation so that the atoms can rearrange in such a way that opposite lone pairs do not directly face each other. Nevertheless, due to the periodic boundary conditions imposed by the computational scheme, geometrical artefacts can be fully avoided either in the limit of very large supercells or by identifying a reasonably small supercell that proves to be an energetic minimum. Pursuing the second strategy, in Figure 2a, we report the relative energy per formula unit (f.u.) of both gC_3N_4-t and gC_3N_4-h, studied in different simulation cells, with respect to an f.u. of flat gC_3N_4-t. The cell parameters and the relative energies per f.u. are reported in the Supporting information. It is evident that, by enlarging the standard unit cell, an energy minimum is reached with the 3×3 supercell. Further expanding the supercell to 4×4 introduces other artificial constraints on the buckling periodicity that result in a higher energy. The 3×3 supercells hence appear to provide a fully relaxed geometry; however, it is possible to notice that the smaller, rotated, $\sqrt{3} \times \sqrt{3}$ cells reported in Figure 1 show the same energy per f.u. and buckling pattern. The phDOS computed for gC_3N_4-t and gC_3N_4-h in the flat 1×1 and $\sqrt{3} \times \sqrt{3}$ cells (c.f. Supporting information, Figure S3) demonstrate that, while the flat geometry is dynamically unstable, the $\sqrt{3} \times \sqrt{3}$ structures do not show soft phonon modes. We also note that, for all considered simulation cells, the heptazine-based allotrope presents a lower energy per formula unit than the corresponding gC_3N_4-t structure, though the stabilization of gC_3N_4-h with respect to gC_3N_4-t, both in $\sqrt{3} \times \sqrt{3}$ geometry, is less than 40 meV/atom. We shall then adopt as equilibrium geometries the $\sqrt{3} \times \sqrt{3}$ structures and compute the electronic and optical properties for both allotropes.

In Figure 3, we report the electronic band structure of gC_3N_4-t (a) and gC_3N_4-h (b) computed in their $\sqrt{3} \times \sqrt{3}$ cell, at the DFT (@DFT), and at the G_0W_0 (@G_0W_0) levels of approximation.
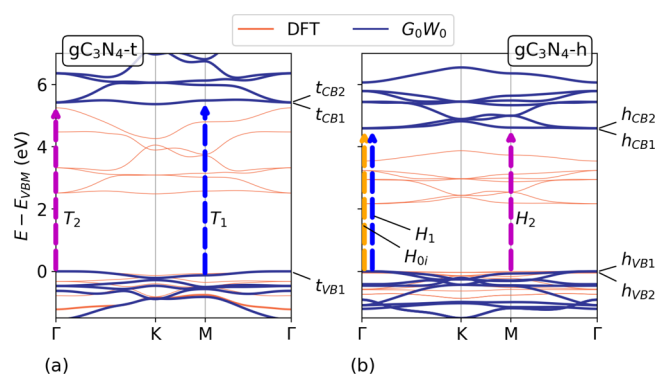
Figure 3. Band structures of $\sqrt{3} \times \sqrt{3}$ gC_3N_4-t (a) and gC_3N_4-h (b), computed at the DFT (thin red lines) and at the G_0W_0 (blue lines) levels of approximation. The dashed vertical arrows mark the electronic transitions contributing to some exciton states obtained by solving the BSE. The arrows in panels (a) and (b) correspond to the crosses in the upper panels of Figure 4a and Figure 4b, respectively.

gC_3N_4-t presents an indirect electronic gap between the valence band maximum, located at the Γ point, and the conduction band minimum at the K point. The indirect gap is computed to be 2.48 eV @DFT and is then widened to 5.37 eV @G_0W_0. The direct gap at the Γ point is only slightly larger, measuring 2.52 eV @DFT and 5.42 eV @G_0W_0. It is possible to notice that the effect of corrugation and stabilization of the structure leads to important changes to the electronic properties. In particular, the stress minimization of the $\sqrt{3} \times \sqrt{3}$ cell results in a slightly indirect gap, as opposed to previous results in the literature.[38,39] It is also worth pointing out that the direct gap obtained from the optimized, buckled structure is more than 1 eV larger than the result for flat geometry,[38] both @DFT and @G_0W_0.

gC_3N_4-h displays a direct electronic gap at the Γ point, 2.17 eV wide @DFT and 4.60 eV @G_0W_0. We note that the QP bandgap of the flat structure was, instead, computed to be indirect, 4.15 eV wide, while the direct bandgap was 2.09 eV @ DFT and 5.22 eV @G_0W_0.[38]

From Figure 3a,b, it is evident that the electronic structures of both gC_3N_4-t and gC_3N_4-h, in the $\sqrt{3} \times \sqrt{3}$ buckled geometry, feature bands that show little dispersion along the Brillouin zone path. This reflects the higher spatial localization of the electronic states imposed by corrugation and, in particular, the breaking of the delocalized π bond that

characterizes the lower conduction band in the flat geometry. When corrugation is considered, the p_z orbitals of C and N, which contribute to the lower conduction band as seen in Figure 2b, cannot create a complete, delocalized π system across the structure but are forced to form much more localized and less stabilized states. The impact of buckling on the electronic band structure can then be regarded as twofold: on the one hand, the destabilization of the states contributed by carbon and nitrogen p_z orbitals, i.e., the lower conduction bands of both gC$_3$N$_4$-t and gC$_3$N$_4$-h, causes the opening of the bandgap already at the DFT level. On the other hand, a higher electronic localization increases the screening and results in a G_0W_0 gap opening which tends to be smaller than what observed in the flat case.

The QP energies computed @G_0W_0 are then employed in the calculation of the optical absorption of both allotropes. In the upper panels of Figure 4a and Figure 4b, we report the
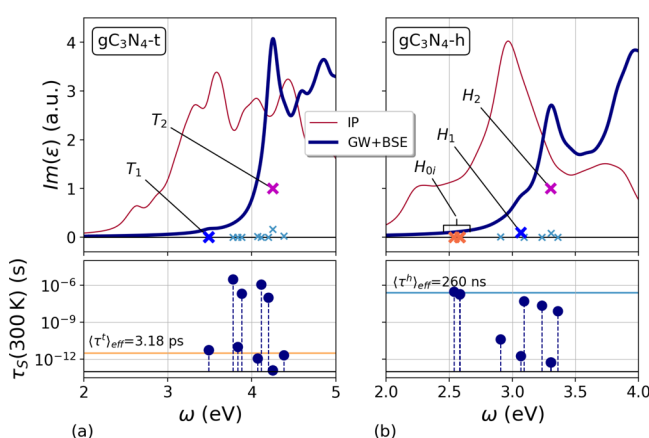
Figure 4. (a, b) Upper panels: imaginary part of the macroscopic dielectric function computed for gC$_3$N$_4$-t and gC$_3$N$_4$-h, respectively, at the independent particle and GW+BSE levels. The crosses mark the excitonic states obtained from the BSE. (a, b) Lower panels: exciton radiative lifetimes of gC$_3$N$_4$-t and gC$_3$N$_4$-h, respectively, at $T = 300$ K. The horizontal lines mark the effective radiative lifetimes $\langle\tau\rangle_{\text{eff}}$.

imaginary part of the macroscopic dielectric function of gC$_3$N$_4$-t and gC$_3$N$_4$-h, respectively, computed with different approaches. The thin red lines show the spectra obtained with the independent-particle (IP) random phase approximation based on the PBE energy levels. The thick blue lines represent the spectra obtained by solving the BSE built by using the QP energies. It is evident that the IP approach, using PBE energetics, largely redshifts the spectra. On the contrary, the solution of the BSE allows one to obtain reliable absorption spectra by taking into account excitonic effects.

In the upper panel of Figure 4a, it is possible to notice that the optical absorption of gC$_3$N$_4$-t shows a pronounced peak at 4.25 eV, related to the T_2 bright exciton. The optical gap, however, is given by the bright T_1 exciton, which also corresponds to the lowest-energy solution of the BSE and is located at 3.49 eV. By analyzing the exciton wavefunctions, it is possible to identify which electronic transitions give the largest contributions. In particular, as marked by the arrows in Figure 3a, T_2 receives significant contributions from transitions around the Γ point between the top valence band (tVB) and the degenerate bottom conduction band (bCB), while T_1 is mostly given by transitions around the M point between the tVB and the non-degenerate bCB. Although the electronic gaps

at Γ and at M differ by less than 0.2 eV, the binding energies of T_1 and T_2 are $E_{T_1}^b = 1.94$ eV and $E_{T_2}^b = 1.18$ eV. Indeed, as shown in Figure 3a, at the Γ point, the bCB is made of two degenerate bands, t_{CB1} and t_{CB2}, one of which, t_{CB2}, shows a larger dispersion along the ΓK direction, while, at M, the bCB is only composed of the almost flat t_{CB1} band. Therefore, around Γ the electronic transitions involve less localized states, which, in turn, yield a smaller screening than more localized states as t_{CB1} around M. A smaller screening implies a reduced direct electron−hole interaction and thus a smaller exciton binding energy, so that $E_{T_1}^b > E_{T_2}^b$. In the lower panel of Figure 4a, we report the exciton radiative lifetimes of the exciton states between T_1 and T_2. Here, we can notice the presence of several dark excitons, with very small dipole strength, with $\tau_S \approx 1$ μs, while $\tau_{T_2} = 0.1$ ps and $\tau_{T_1} = 3.1$ ps. The thermal average favors the lowest energy states so that the effective radiative lifetime of gC$_3$N$_4$-t is dictated by the lifetime of T_1 and, at $T = 300$ K, results in $\langle\tau^t\rangle_{\text{eff}} = 3.18$ ps.

The absorption spectrum and excitonic properties of gC$_3$N$_4$-h, the upper panel of Figure 4b, look richer. In the lowest part of the spectrum, we notice the presence of a closely spaced triplet of excitons H_{0i}, with $i = a, b, c$. These are all dark, and the lowest-energy exciton, H_{0a}, is located at 2.57 eV. As shown in Figure 3b, the tVB of gC$_3$N$_4$-h around the Γ point is composed of two degenerate bands, h_{VB1} and h_{VB2} and, likewise, the bCB is given by the degenerate h_{CB1} and h_{CB2} bands. The dark excitons H_{0i} are mainly composed of transitions around the Γ point involving h_{VB1} and h_{CB1}, which are dipole-forbidden. The first bright exciton, responsible for a noticeable bump in the spectrum, is H_1 at 3.08 eV, mainly due to transitions between h_{VB1} and h_{CB2} around Γ, while at 3.30 eV, we find H_2, which forms the first strong absorption peak and receives the largest contributions from transitions between h_{VB1} and h_{CB1} around the M point.

Some comments on this complex exciton pattern are in order. Excitons H_{0i} and H_1 receive contributions from transitions between bands that are degenerate in energy; nonetheless, their binding energies are largely different, e.g., $E_{H_{0a}}^b = 2.03$ eV and $E_{H_1}^b = 1.52$ eV. This discrepancy can again be traced back to differences in the direct electron−hole interaction in the two cases. As shown Figure 2b, the tVB of gC$_3$N$_4$-h receives significant contributions from N p_z orbitals and so does the h_{VB1} state at the Γ point ($h_{\text{VB1}}@\Gamma$). bCB states $h_{\text{CB1}}@\Gamma$ and $h_{\text{CB2}}@\Gamma$ both result from C and N p_z orbitals, but their spatial localizations differ from each other (cf. Supporting Information). For this reason, the overlap between $h_{\text{VB1}}@\Gamma$ and $h_{\text{CB1}}@\Gamma$ is large and screening plays a significant role, giving the particularly large exciton binding energy of H_{0i}, while the overlap between $h_{\text{VB1}}@\Gamma$ and $h_{\text{CB2}}@\Gamma$ is small so that $E_{H_{0i}}^b > E_{H_1}^b$. Similar considerations can be drawn for H_2 (cf. Supporting Information) given that the electronic bandgap at M differs from the gap at Γ only by some meV, while $E_{H_{0i}}^b > E_{H_3}^b = 1.51$ eV.

It is important to notice that, as evident from Figure 4b, the optical absorption edge, around H_1, falls in the blue-violet part of the visible spectrum, as opposed to the gC$_3$N$_4$-t case, cf. Figure 4a, in which the absorption onset, marked by T_1, is already in the near ultraviolet. The absorption edge value of gC$_3$N$_4$-h obtained in this work, $\sim$3 eV, is in line with the experimental optical gap measurement of $\sim$2.7 eV,[93,94] provided one considers that the absorption measurements
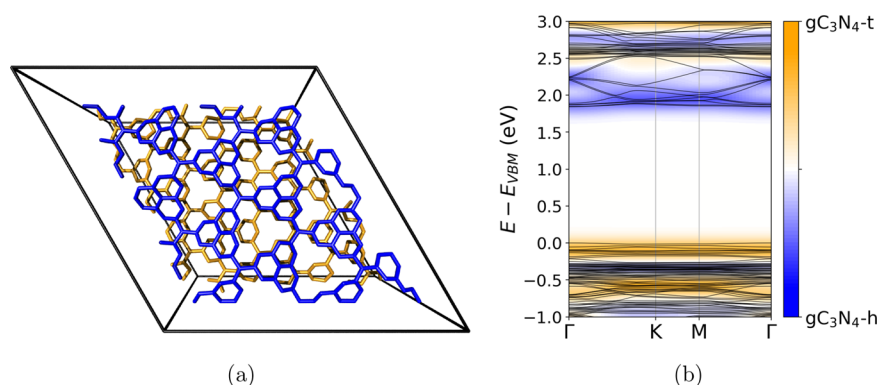
Figure 5. (a) Perspective view of the gC_3N_4-t/gC_3N_4-h vdW heterostructure. The gC_3N_4-t and gC_3N_4-h layers are represented by orange and blue segments, respectively. The periodic cell is marked by the black lines. (b) Heterostructure electronic bands and k-resolved DOS. Bands are colored according to the layer whose atomic orbitals contribute the most. The blue color marks contributions from gC_3N_4-h atoms only, white equal contributions from both layers, while orange signals contributions from gC_3N_4-t atoms only.

are carried out on layered systems. Indeed, a larger optical gap is expected in single-layer 2D samples, as in our study, in comparison to bulk or few-layer materials such those experimentally explored.[36]

In the lower panel of Figure 4b, we report the radiative lifetimes of the exciton states up to around H_2. As in the case of gC_3N_4-t, we can notice several dark states; however, the crucial property of gC_3N_4-h is the presence of the three dark excitons H_{0i} as lowest-energy states. Their lifetimes are $\tau_{H_{0i}} \simeq$ 200 ns, while $\tau_{H_2} = 0.5$ ps. The thermal average is dominated by the lifetimes of the lowest-energy states; therefore, at $T =$ 300 K, we obtain $\langle \tau^h \rangle = 260$ ns. Since the bottom of the gC_3N_4-h exciton spectrum is composed of dark states, when thermalization is assumed, these long-lived levels become highly populated and the system remains in an excited state for a rather long period of time. Heptazine-based graphitic carbon nitride has indeed shown remarkably long exciton lifetimes in various experiments, mainly involving the nanosheet form. In ref 31, by means of time-resolved measurements of decay spectra, Dong et al. obtained an average lifetime of the photogenerated electrons and holes of around 37 ns in nanosheets (16 nm-thick). Similar results were collected by Choudhury et al., which, in ref 33, measured an average lifetime of about 20 ns in graphitic C_3N_4 nanosheets composed of more than 10 atomic layers. Niu et al. pointed out in ref 29 that the average exciton lifetime in graphitic C_3N_4 decreases when increasing the thickness of the sample due to quantum confinement effects, which become stronger when dimensionality is reduced. Therefore, by considering the differences in thickness and defectivity between our graphene-like monatomic layer and the experimentally studied few-layer nanosheets, we argue that our results can provide a reliable theoretical prediction on the order of magnitude of the effective exciton radiative lifetime in gC_3N_4-h.

Finally, aiming at suggesting possible strategies to favor exciton dissociation, we focus on a vertical vdW heterostructure made of gC_3N_4-t and gC_3N_4-h layers. The heterostructure relaxed geometry is reported in Figure 5a, where the gC_3N_4-t and gC_3N_4-h layers are represented by the orange and blue nets, respectively. The strain along the lattice vectors is around 1.5% with respect to the equilibrium lattice parameters of the single layers and the cohesion energy is −24 meV/Å^2, with respect to the separate layers. The intriguing features of the heterostructure come to light with the analysis

of its electronic band structure. In Figure 5b, we show the band structure computed @DFT. Though affected by the notorious limitations, this approach is more than sufficient for the purpose of gaining a qualitative insight on the heterostructure properties. To the band plot, we superimpose the k-resolved DOS projected on the orbitals of the atoms composing the two layers. This way, the bands along the k path are colored according to the difference between the DOS contributions from the two layers, allowing us to identify whether the electronic states at various k points are localized on the gC_3N_4-t layer, or on the gC_3N_4-h layer, or on both. The heterostructure bandgap is 1.84 eV @DFT, smaller than both gC_3N_4-t and gC_3N_4-h single layers, showing the effect of the interaction between the two layers. Moreover, it is evident from Figure 5b that the upper valence band is given by states localized on the gC_3N_4-t layer, while the lower conduction band appears localized on gC_3N_4-h, realizing a type-II band alignment. Although a detailed study of different stacking patterns is needed to pinpoint the most stable heterostructure geometry, we expect that the main feature of a type-II band alignment will not be affected due to the weak interaction between the two layers. It is then conceivable that either a direct transition between tVB and bCB occurs, leaving the hole on the gC_3N_4-t layer and promoting the electron on gC_3N_4-h, or, should the dipole strength of the direct transition vanish, an indirect, phonon-mediated, mechanism takes place, leading to the same final result.[95,96] Indeed, when considering vdW heterostructures, transitions between states belonging to different layers are very often suppressed due to the scarce overlap of the relative electronic states. However, even in the case of optical transitions taking place between two gC_3N_4-h states, the type-II band alignment is such that the system is at its energetic minimum only when the hole occupies the valence band maximum, located on gC_3N_4-t. It has been shown[97,98] that this final state can be efficiently reached through tunneling and the emission of phonons with suitable energy and momentum, which make the system relax to its energy minimum, thus enhancing the exciton lifetime and charge separation.[99]

4. CONCLUSIONS

In this work, we have presented a thorough analysis of various properties of the increasingly widespread two-dimensional graphene-like carbon nitride. The features that make this

material attractive for new technological applications are mainly related to its optical absorption and exciton fine structure. These, in turn, are extremely sensitive to the geometry, dimensionality, and strain of the material. For these reasons, a stability analysis of different corrugation geometries has been carried out, highlighting the fundamental role of buckling and pointing at the $\sqrt{3} \times \sqrt{3}$ cell as the most stable geometry for both allotropes.

Only once these stable structures have been identified, it is possible to reliably discuss the electronic properties at the G_0W_0 level, identifying rather large bandgaps of the order of 5 eV. In particular, the bandgap of gC$_3$N$_4$-t in our buckled $\sqrt{3} \times \sqrt{3}$ cell turns out slightly indirect and larger than the direct bandgap of gC$_3$N$_4$-h. The QP levels have allowed us to compute the optical absorption spectra of both allotropes by solving the BSE and revealing their exciton patterns. In both cases, large exciton binding energies have been computed, in line with the existing literature. While gC$_3$N$_4$-t shows an absorption edge in the near UV region and no low-energy dark excitons, the absorption edge of gC$_3$N$_4$-h falls in the blue-violet part of the visible spectrum and dark excitons are present at a lower energy. These properties directly impact on the viability of gC$_3$N$_4$-h in optoelectronics, photovoltaics, and photocatalysis. Although absorption occurs in an energy window in which the intensity of the solar spectrum is modest, the presence of dark excitons as lowest-energy states largely affects the average radiative lifetime, lifting it to 260 ns. This long excitation lifetime dramatically increases the probability that the photogenerated electrons and holes contribute to photocatalytic reactions before recombination. In addition, single layer gC$_3$N$_4$-h may represent an interesting material in optoelectronics, appearing particularly promising from the perspective of exciton devices, in which long-lived excitons are required.

Finally, we have proposed a novel vdW heterostructure containing one layer of each allotrope. We have predicted a type-II band alignment between the two materials, with the heterostructure tVB consisting of electronic states localized on gC$_3$N$_4$-t and the bCB localized on gC$_3$N$_4$-h. This appears particularly promising for enhanced charge separation between the two layers, achieved either by direct photoexcitation or through the polarization-to-population mechanism.[98]

In conclusion, these results shed light on this promising bidimensional material and can serve as a guide to understanding gC$_3$N$_4$ peculiar properties and designing novel applications that best exploit its predicted features.

ASSOCIATED CONTENT

Ⓢ Supporting Information

The Supporting Information is available free of charge at https://pubs.acs.org/doi/10.1021/acsanm.0c03317.

> Details on the DFT, G_0W_0, and BSE calculations; energetic, structural, and vibrational data of studied supercells, and wavefunctions of selected states (PDF)

AUTHOR INFORMATION

Corresponding Author

Michele Re Fiorentin − *Center for Sustainable Future Technologies, Istituto Italiano di Tecnologia, Torino 10144, Italy;* Ⓞ orcid.org/0000-0002-1074-0411; Email: michele.refiorentin@iit.it

Authors

Francesca Risplendi − *Dipartimento di Scienza Applicata e Tecnologia, Politecnico di Torino, Torino 10129, Italy;* Ⓞ orcid.org/0000-0002-1277-6733

Maurizia Palummo − *Dipartimento di Fisica and INFN, Università di Roma "Tor Vergata", Roma 00133, Italy;* Ⓞ orcid.org/0000-0002-3097-8523

Giancarlo Cicero − *Dipartimento di Scienza Applicata e Tecnologia, Politecnico di Torino, Torino 10129, Italy;* Ⓞ orcid.org/0000-0002-2920-9882

Complete contact information is available at:
https://pubs.acs.org/10.1021/acsanm.0c03317

Notes

The authors declare no competing financial interest.

ACKNOWLEDGMENTS

REFERENCES

(1) Wang, X.; Maeda, K.; Thomas, A.; Takanabe, K.; Xin, G.; Carlsson, J. M.; Domen, K.; Antonietti, M. A metal-free polymeric photocatalyst for hydrogen production from water under visible light. *Nat. Mater.* **2009**, *8*, 76−80.

(2) Liang, X.; Wu, C.-M. L. Metal-free two-dimensional phosphorus carbide as an efficient electrocatalyst for hydrogen evolution reaction comparable to platinum. *Nano Energy* **2020**, *71*, 104603.

(3) Zhang, W.; Yin, J.; Zhang, P.; Tang, X.; Ding, Y. Two-dimensional phosphorus carbide as a promising anode material for lithium-ion batteries. *J. Mater. Chem. A* **2018**, *6*, 12029−12037.

(4) Guo, X.-N.; Tong, X.-L.; Guo, X.-Y. *Novel Carbon Materials and Composites*; John Wiley & Sons, Ltd: 2019; Chapter 2, pp. 35−72.

(5) Kandy, M. M. Carbon-based photocatalysts for enhanced photocatalytic reduction of CO$_2$ to solar fuels. *Sustainable Energy Fuels* **2020**, *4*, 469−484.

(6) Liu, A. Y.; Cohen, M. L. Prediction of New Low Compressibility Solids. *Science* **1989**, *245*, 841−842.

(7) Gong, Y.; Li, M.; Li, H.; Wang, Y. Graphitic carbon nitride polymers: promising catalysts or catalyst supports for heterogeneous oxidation and hydrogenation. *Green Chem.* **2015**, *17*, 715−736.

(8) Wang, Z.; Hu, X.; Zou, G.; Huang, Z.; Tang, Z.; Liu, Q.; Hu, G.; Geng, D. Advances in constructing polymeric carbon-nitride-based nanocomposites and their applications in energy chemistry. *Sustainable Energy Fuels* **2019**, *3*, 611−655.

(9) Li, Y.; Li, X.; Zhang, H.; Xiang, Q. Porous graphitic carbon nitride for solar photocatalytic applications. *Nanoscale Horiz.* **2020**, *5*, 765−786.

(10) Monai, M.; Melchionna, M.; Fornasiero, P. From metal to metal-free catalysts: Routes to sustainable chemistry. In *Advances in catalysis*; Song, C., Ed.; Academic Press: 2018; Vol. 63; pp. 1−73, DOI: 10.1016/bs.acat.2018.10.001.

(11) Li, C.; Xu, Y.; Tu, W.; Chen, G.; Xu, R. Metal-free photocatalysts for various applications in energy conversion and environmental purification. *Green Chem.* **2017**, *19*, 882−899.

(12) Su, D. S.; Zhang, J.; Frank, B.; Thomas, A.; Wang, X.; Paraknowitsch, J.; Schlögl, R. Metal-Free Heterogeneous Catalysis for Sustainable Chemistry. *ChemSusChem* **2010**, *3*, 169−180.

(13) Ramli, Z. A. C.; Kamarudin, S. K. Platinum-Based Catalysts on Various Carbon Supports and Conducting Polymers for Direct Methanol Fuel Cell Applications: a Review. *Nanoscale Res. Lett.* **2018**, *13*, 410.

(14) Yin, H.-J.; Zhou, J.-H.; Zhang, Y.-W. Shaping well-defined noble-metal-based nanostructures for fabricating high-performance electrocatalysts: advances and perspectives. *Inorg. Chem. Front.* **2019**, *6*, 2582−2618.

(15) Garino, N.; Castellino, M.; Sacco, A.; Risplendi, F.; Muñoz-Tabares, J. A.; Armandi, M.; Chiodoni, A.; Salomon, D.; Quaglio, M.; Pirri, C. F.; Cicero, G. Proving the existence of Mn porphyrin-like complexes hosted in reduced graphene oxide with outstanding performance as oxygen reduction reaction catalysts. *2D Mater.* **2019**, *6*, No. 045001.

(16) Risplendi, F.; Re Fiorentin, M.; Cicero, G. Unravelling electrocatalytic properties of metal porphyrin-like complexes hosted in graphene matrices. *2D Mater.* **2020**, *7*, No. 025017.

(17) Zeng, J.; Bejtka, K.; Di Martino, G.; Sacco, A.; Castellino, M.; Re Fiorentin, M.; Risplendi, F.; Farkhondehfal, M. A.; Hernández, S.; Cicero, G.; Pirri, C. F.; Chiodoni, A. Microwave-Assisted Synthesis of Copper-Based Electrocatalysts for Converting Carbon Dioxide to Tunable Syngas. *ChemElectroChem* **2020**, *7*, 229−238.

(18) Garino, N.; Zeng, J.; Castellino, M.; Sacco, A.; Risplendi, F.; Fiorentin, M. R.; Bejtka, K.; Chiodoni, A.; Salomon, D.; Segura-Ruiz, J.; Pirri, C. F.; Cicero, G. Facilely synthesized nitrogen-doped reduced graphene oxide functionalized with copper ions as electrocatalyst for oxygen reduction. *npj 2D Mater.Appl.* **2021**, *5*, 2.

(19) Pickard, C. J.; Salamat, A.; Bojdys, M. J.; Needs, R. J.; McMillan, P. F. Carbon nitride frameworks and dense crystalline polymorphs. *Phys. Rev. B* **2016**, *94*, No. 094104.

(20) Fan, Q.; Chai, C.; Wei, Q.; Yang, Y. Two Novel C_3N_4 Phases: Structural, Mechanical and Electronic Properties. *Materials* **2016**, *9*, 427.

(21) Sun, P.; He, C.; Zhang, C.; Xiao, H.; Zhong, J. First-principles prediction of three new graphitic C_3N_4 allotropes with potentials for application in sun-light-driven water splitting. *Phys. B* **2019**, *562*, 131−134.

(22) Zhu, J.; Wei, Y.; Chen, W.; Zhao, Z.; Thomas, A. Graphitic carbon nitride as a metal-free catalyst for NO decomposition. *Chem. Commun.* **2010**, *46*, 6965−6967.

(23) Bojdys, M. J.; Severin, N.; Rabe, J. P.; Cooper, A. I.; Thomas, A.; Antonietti, M. Exfoliation of Crystalline 2D Carbon Nitride: Thin Sheets, Scrolls and Bundles via Mechanical and Chemical Routes. *Macromol. Rapid Commun.* **2013**, *34*, 850−854.

(24) Ma, T. Y.; Tang, Y.; Dai, S.; Qiao, S. Z. Proton-Functionalized Two-Dimensional Graphitic Carbon Nitride Nanosheet: An Excellent Metal-/Label-Free Biosensing Platform. *Small* **2014**, *10*, 2382−2389.

(25) Zheng, Y.; Liu, J.; Liang, J.; Jaroniec, M.; Qiao, S. Z. Graphitic carbon nitride materials: controllable synthesis and applications in fuel cells and photocatalysis. *Energy Environ. Sci.* **2012**, *5*, 6717−6731.

(26) Wang, X.; Blechert, S.; Antonietti, M. Polymeric Graphitic Carbon Nitride for Heterogeneous Photocatalysis. *ACS Catal.* **2012**, *2*, 1596−1606.

(27) Melissen, S.; Le Bahers, T.; Steinmann, S. N.; Sautet, P. Relationship between Carbon Nitride Structure and Exciton Binding Energies: A DFT Perspective. *J. Phys. Chem C* **2015**, *119*, 25188−25196.

(28) Wang, H.; Jiang, S.; Chen, S.; Zhang, X.; Shao, W.; Sun, X.; Zhao, Z.; Zhang, Q.; Luo, Y.; Xie, Y. Insights into the excitonic processes in polymeric photocatalysts. *Chem. Sci.* **2017**, *8*, 4087−4092.

(29) Niu, P.; Zhang, L.; Liu, G.; Cheng, H.-M. Graphene-Like Carbon Nitride Nanosheets for Improved Photocatalytic Activities. *Adv. Funct. Mater.* **2012**, *22*, 4763−4770.

(30) Merschjann, C.; Tyborski, T.; Orthmann, S.; Yang, F.; Schwarzburg, K.; Lublow, M.; Lux-Steiner, M.-C.; Schedel-Niedrig, T. Photophysics of polymeric carbon nitride: An optical quasimonomer. *Phys. Rev. B* **2013**, *87*, 205204.

(31) Dong, F.; Li, Y.; Wang, Z.; Ho, W.-K. Enhanced visible light photocatalytic activity and oxidation ability of porous graphene-like g-C_3N_4 nanosheets via thermal exfoliation. *Appl. Surf. Sci.* **2015**, *358*, 393−403 Graphene and C_3N_4-based Photocatalysts.

(32) Gan, Z.; Shan, Y.; Chen, J.; Gui, Q.; Zhang, Q.; Nie, S.; Wu, X. The origins of the broadband photoluminescence from carbon nitrides and applications to white light emitting. *Nano Res.* **2016**, *9*, 1801−1812.

(33) Choudhury, B.; Paul, K. K.; Sanyal, D.; Hazarika, A.; Giri, P. K. Evolution of Nitrogen-Related Defects in Graphitic Carbon Nitride Nanosheets Probed by Positron Annihilation and Photoluminescence Spectroscopy. *J Phys. Chem. C* **2018**, *122*, 9209−9219.

(34) Li, Y.; Jin, S.; Xu, X.; Wang, H.; Zhang, X. Excitonic effects on photophysical processes of polymeric carbon nitride. *J. Appl. Phys.* **2020**, *127*, 170903.

(35) Xu, Y.; Gao, S.-P. Band gap of C3N4 in the GW approximation. *Int. J. Hydrogen Energy* **2012**, *37*, 11072−11080 Hydrogen Enriched Methane.

(36) Espinosa-García, W. F.; Osorio-Guillén, J. M.; Araujo, C. M. Dimension-dependent band alignment and excitonic effects in graphitic carbon nitride: a many-body perturbation and time-dependent density functional theory study. *RSC Adv.* **2017**, *7*, 44997−45002.

(37) Osorio-Guillén, J. M.; Espinosa-García, W. F.; Moyses Araujo, C. Assessing photocatalytic power of g-C_3N_4 for solar fuel production: A first-principles study involving quasi-particle theory and dispersive forces. *J. Chem. Phys.* **2015**, *143*, No. 094705.

(38) Wei, W.; Jacob, T. Strong excitonic effects in the optical properties of graphitic carbon nitride g-C_3N_4 from first principles. *Phys. Rev. B* **2013**, *87*, No. 085202.

(39) Steinmann, S. N.; Melissen, S. T. A. G.; Le Bahers, T.; Sautet, P. Challenges in calculating the bandgap of triazine-based carbon nitride structures. *J. Mater. Chem. A* **2017**, *5*, 5115−5122.

(40) Sun, J.; Li, X.; Yang, J. The roles of buckled geometry and water environment in the excitonic properties of graphitic C_3N_4. *Nanoscale* **2018**, *10*, 3738−3743.

(41) Gracia, J.; Kroll, P. Corrugated layered heptazine-based carbon nitride: the lowest energy modifications of C_3N_4 ground state. *J. Mater. Chem.* **2009**, *19*, 3013−3019.

(42) Azofra, L. M.; MacFarlane, D. R.; Sun, C. A DFT study of planar vs. corrugated graphene-like carbon nitride (g-C_3N_4) and its role in the catalytic performance of CO2 conversion. *Phys. Chem. Chem. Phys.* **2016**, *18*, 18507−18514.

(43) Deifallah, M.; McMillan, P. F.; Corà, F. Electronic and Structural Properties of Two-Dimensional Carbon Nitride Graphenes. *J Phys. Chem. C* **2008**, *112*, 5447−5453.

(44) Zhang, Z.; Qian, Q.; Li, B.; Chen, K. J. Interface Engineering of Monolayer MoS$_2$/GaN Hybrid Heterostructure: Modified Band Alignment for Photocatalytic Water Splitting Application by Nitridation Treatment. *ACS Appl. Mater. Interfaces* **2018**, *10*, 17419−17426.

(45) Hedin, L. New Method for Calculating the One-Particle Green's Function with Application to the Electron-Gas Problem. *Phys. Rev.* **1965**, *139*, A796−A823.

(46) Hybertsen, M. S.; Louie, S. G. Electron correlation in semiconductors and insulators: Band gaps and quasiparticle energies. *Phys. Rev. B* **1986**, *34*, 5390−5413.

(47) Onida, G.; Reining, L.; Rubio, A. Electronic excitations: density-functional versus many-body Green's-function approaches. *Rev. Mod. Phys.* **2002**, *74*, 601−659.

(48) Salpeter, E. E.; Bethe, H. A. A Relativistic Equation for Bound-State Problems. *Phys. Rev.* **1951**, *84*, 1232−1242.

(49) Albrecht, S.; Reining, L.; Del Sole, R.; Onida, G. *Ab Initio* Calculation of Excitonic Effects in the Optical Spectra of Semiconductors. *Phys. Rev. Lett.* **1998**, *80*, 4510−4513.

(50) Palummo, M.; Bernardi, M.; Grossman, J. C. Exciton Radiative Lifetimes in Two-Dimensional Transition Metal Dichalcogenides. *Nano Lett.* **2015**, *15*, 2794−2800.

(51) Chen, H.-Y.; Jhalani, V. A.; Palummo, M.; Bernardi, M. *Ab initio* calculations of exciton radiative lifetimes in bulk crystals, nanostructures, and molecules. *Phys. Rev. B* **2019**, *100*, No. 075135.

(52) Xu, M.; Gao, Y.; Moreno, E. M.; Kunst, M.; Muhler, M.; Wang, Y.; Idriss, H.; Wöll, C. Photocatalytic Activity of Bulk TiO$_2$ Anatase

and Rutile Single Crystals Using Infrared Absorption Spectroscopy. *Phys. Rev. Lett.* **2011**, *106*, 138302.

(53) Ohtani, B. Titania Photocatalysis beyond Recombination: A Critical Review. *Catalysts* **2013**, *3*, 942−953.

(54) Hu, L.; Xu, C.; Peng, L.; Gu, F. L.; Yang, W. Photocatalytic activity and the radiative lifetimes of excitons via an *ab initio* approach. *J. Mater. Chem. A* **2018**, *6*, 15027−15032.

(55) Miller, B.; Steinhoff, A.; Pano, B.; Klein, J.; Jahnke, F.; Holleitner, A.; Wurstbauer, U. Long-Lived Direct and Indirect Interlayer Excitons in van der Waals Heterostructures. *Nano Lett.* **2017**, *17*, 5229−5237.

(56) Liu, Y.; Dini, K.; Tan, Q.; Liew, T.; Novoselov, K. S.; Gao, W. Electrically controllable router of interlayer excitons. *Sci. Adv.* **2020**, *6*, eaba1830.

(57) Unuchek, D.; Ciarrocchi, A.; Avsar, A.; Watanabe, K.; Taniguchi, T.; Kis, A. Room-temperature electrical control of exciton flux in a van der Waals heterostructure. *Nature* **2018**, *560*, 340−344.

(58) Uda, T.; Yoshida, M.; Ishii, A.; Kato, Y. K. Electric-Field Induced Activation of Dark Excitonic States in Carbon Nanotubes. *Nano Lett.* **2016**, *16*, 2278−2282.

(59) Cong, K.; Noe, G. T., II; Kono, J. *Excitons in magnetic fields. Encyclopedia of Modern Optics*; 2nd Ed.; Elsevier: Oxford, 2018; pp. 63−81.

(60) Starukh, H.; Praus, P. Doping of Graphitic Carbon Nitride with Non-Metal Elements and Its Applications in Photocatalysis. *Catalysts* **2020**, *10*, 1119.

(61) Hasija, V.; Raizada, P.; Sudhaik, A.; Sharma, K.; Kumar, A.; Singh, P.; Jonnalagadda, S. B.; Thakur, V. K. Recent advances in noble metal free doped graphitic carbon nitride based nanohybrids for photocatalysis of organic contaminants in water: A review. *Appl. Mater. Today* **2019**, *15*, 494−524.

(62) Wang, H.; Sun, X.; Li, D.; Zhang, X.; Chen, S.; Shao, W.; Tian, Y.; Xie, Y. Boosting Hot-Electron Generation: Exciton Dissociation at the Order−Disorder Interfaces in Polymeric Photocatalysts. *J. Am. Chem. Soc.* **2017**, *139*, 2468−2473.

(63) Ran, J.; Guo, W.; Wang, H.; Zhu, B.; Yu, J.; Qiao, S.-Z. Metal-Free 2D/2D Phosphorene/g-C_3N_4 Van der Waals Heterojunction for Highly Enhanced Visible-Light Photocatalytic H_2 Production. *Adv. Mater.* **2018**, *30*, 1800128.

(64) Wang, H.; Liu, W.; He, X.; Zhang, P.; Zhang, X.; Xie, Y. An Excitonic Perspective on Low-Dimensional Semiconductors for Photocatalysis. *J. Am. Chem. Soc.* **2020**, *142*, 14007−14022 PMID: 32702981.

(65) Wang, H.; Jin, S.; Zhang, X.; Xie, Y. Excitonic Effects in Polymeric Photocatalysts. *Am. Ethnol.* **2020**, 23024−23035.

(66) Wang, A.; Wang, C.; Fu, L.; Wong-Ng, W.; Lan, Y. Recent Advances of Graphitic Carbon Nitride-Based Structures and Applications in Catalyst, Sensing, Imaging, and LEDs. *Nano-Micro Lett.* **2017**, *9*, 47.

(67) Noda, Y.; Merschjann, C.; Tarábek, J.; Amsalem, P.; Koch, N.; Bojdys, M. J. Directional Charge Transport in Layered Two-Dimensional Triazine-Based Graphitic Carbon Nitride. *Angew. Chem. Int. Ed.* **2019**, *58*, 9394−9398.

(68) Grosso, G.; Graves, J. C.; Hammack, A.; High, A.; Butov, L.; Hanson, M.; Gossard, A. Excitonic Switches Operating at Around 100 K. In *Quantum Electronics and Laser Science Conference*; Optical Society of America: 2010; *2010*; p QFI5.

(69) Andreakou, P.; Poltavtsev, S. V.; Leonard, J. R.; Calman, E. V.; Remeika, M.; Kuznetsova, Y. Y.; Butov, L. V.; Wilkes, J.; Hanson, M.; Gossard, A. C. Optically controlled excitonic transistor. *Appl. Phys. Lett.* **2014**, *104*, No. 091101.

(70) Jin, H.; Guo, C.; Liu, X.; Liu, J.; Vasileff, A.; Jiao, Y.; Zheng, Y.; Qiao, S.-Z. Emerging Two-Dimensional Nanomaterials for Electrocatalysis. *Chem. Rev.* **2018**, *118*, 6337−6408.

(71) Younis, M. A.; Lyu, S.; Zhao, Q.; Lei, C.; Zhang, P.; Yang, B.; Li, Z.; Lei, L.; Hou, Y.; Feng, X. Noble metal-free two dimensional carbon-based electrocatalysts for water splitting. *BMC Mater.* **2019**, *1*, 6.

(72) Tang, S.; Zhu, Y.; Li, H.; Xu, H.; Yuan, S. Two-dimensional carbon nitride-based composites for photocatalytic hydrogen evolution. *Int. J. Hydrogen Energy* **2019**, *44*, 30935−30948.

(73) Zhang, L.; Ding, N.; Wu, J.; Iwasaki, K.; Lin, L.; Yamaguchi, Y.; Shibayama, Y.; Shi, J.; Wu, H.; Luo, Y.; Nakata, K.; Li, D.; Wang, X.; Fujishima, A.; Meng, Q. New two-dimensional porous graphitic carbon nitride nanosheets for highly efficient photocatalytic hydrogen evolution under visible-light irradiation. *Catal. Sci. Technol.* **2018**, *8*, 3846−3852.

(74) Zhao, G.; Yang, H.; Liu, M.; Xu, X. Metal-Free Graphitic Carbon Nitride Photocatalyst Goes Into Two-Dimensional Time. *Front. Chem.* **2018**, *6*, 551.

(75) Kong, L.; Song, P.; Ma, F.; Sun, M. Graphitic carbon nitride-based 2D catalysts for green energy: Physical mechanism and applications. *Mater. Today Energy* **2020**, *17*, 100488.

(76) Giannozzi, P.; et al. QUANTUM ESPRESSO: a modular and open-source software project for quantum simulations of materials. *J. Phys.: Condens. Matter* **2009**, *21*, 395502.

(77) Giannozzi, P.; et al. Advanced Capabilities for Materials Modelling With Quantum ESPRESSO. *J. Phys.: Condens. Matter* **2017**, *29*, 490.

(78) Perdew, J. P.; Burke, K.; Wang, Y. Generalized gradient approximation for the exchange-correlation hole of a many-electron system. *Phys. Rev. B* **1996**, *54*, 16533−16539.

(79) Schlipf, M.; Gygi, F. Optimization algorithm for the generation of ONCV pseudopotentials. *Comput. Phys. Commun.* **2015**, *196*, 36−44.

(80) Monkhorst, H. J.; Pack, J. D. Special points for Brillouin-zone integrations. *Phys. Rev. B* **1976**, *13*, 5188−5192.

(81) Grimme, S. Semiempirical GGA-type density functional constructed with a long-range dispersion correction. *J. Comput. Chem.* **2006**, *27*, 1787−1799.

(82) Malyi, O. I.; Sopiha, K. V.; Persson, C. Energy, Phonon, and Dynamic Stability Criteria of Two-Dimensional Materials. *ACS Appl. Mater. Interfaces* **2019**, *11*, 24876−24884.

(83) Togo, A.; Tanaka, I. First principles phonon calculations in materials science. *Scr. Mater.* **2015**, *108*, 1−5.

(84) Marini, A.; Hogan, C.; Grüning, M.; Varsano, D. yambo: An *ab initio* tool for excited state calculations. *Comput. Phys. Commun.* **2009**, *180*, 1392−1403.

(85) Sangalli, D.; et al. Many-body perturbation theory calculations using the yambo code. *J. Phys.: Condens. Matter* **2019**, *31*, 325902.

(86) Bruneval, F.; Gonze, X. Accurate *GW* self-energies in a plane-wave basis using only a few empty states: Towards large systems. *Phys. Rev. B* **2008**, *78*, No. 085125.

(87) Re Fiorentin, M.; Cicero, G.; Palummo, M. Spatially indirect excitons in black and blue phosphorene double layers. *Phys. Rev. Mater.* **2020**, *4*, No. 074009.

(88) Tamm, I. *Selected Papers*; Bolotovskii, B. M., Frenkel, V. Y., Peierls, R., Eds.; Springer Berlin Heidelberg: Berlin, Heidelberg, 1991; pp. 157−174.

(89) Dancoff, S. M. Non-Adiabatic Meson Theory of Nuclear Forces. *Phys. Rev.* **1950**, *78*, 382−385.

(90) Spataru, C. D.; Ismail-Beigi, S.; Capaz, R. B.; Louie, S. G. Theory and *Ab Initio* Calculation of Radiative Lifetime of Excitons in Semiconducting Carbon Nanotubes. *Phys. Rev. Lett.* **2005**, *95*, 247402.

(91) Perebeinos, V.; Tersoff, J.; Avouris, P. Radiative Lifetime of Excitons in Carbon Nanotubes. *Nano Lett.* **2005**, *5*, 2495−2499.

(92) Lazić, P. *CellMatch*: Combining two unit cells into a common supercell with minimal strain. *Comput. Phys. Commun.* **2015**, *197*, 324−334.

(93) Thomas, A.; Fischer, A.; Goettmann, F.; Antonietti, M.; Müller, J.-O.; Schlögl, R.; Carlsson, J. M. Graphitic carbon nitride materials: variation of structure and morphology and their use as metal-free catalysts. *J. Mater. Chem.* **2008**, *18*, 4893−4908.

(94) Khabashesku, V. N.; Zimmerman, J. L.; Margrave, J. L. Powder Synthesis and Characterization of Amorphous Carbon Nitride. *Chem. Mater.* **2000**, *12*, 3264−3270.

(95) Brem, S.; Selig, M.; Berghaeuser, G.; Malic, E. Exciton Relaxation Cascade in two-dimensional Transition Metal Dichalcogenides. *Sci. Rep.* **2018**, *8*, 8238.

(96) Shulenburger, L.; Baczewski, A. D.; Zhu, Z.; Guan, J.; Tománek, D. The Nature of the Interlayer Interaction in Bulk and Few-Layer Phosphorus. *Nano Lett.* **2015**, *15*, 8170−8175.

(97) Kira, M.; Koch, S. W. Many-body correlations and excitonic effects in semiconductor spectroscopy. *Prog. Quantum Electron.* **2006**, *30*, 155−296.

(98) Selig, M.; Berghäuser, G.; Richter, M.; Bratschitsch, R.; Knorr, A.; Malic, E. Dark and bright exciton formation, thermalization, and photoluminescence in monolayer transition metal dichalcogenides. *2D Mater.* **2018**, *5*, No. 035017.

(99) Ovesen, S.; Brem, S.; Linderälv, C.; Kuisma, M.; Korn, T.; Erhart, P.; Selig, M.; Malic, E. Interlayer exciton dynamics in van der Waals heterostructures. *Commun. Phys.* **2019**, *2*, 23.